Kuwait Journal of Science 51 (2024) 100200

Contents lists available at ScienceDirect

Kuwait Journal of Science

journal homepage: www.sciencedirect.com/journal/kuwait-journal-of-science

Full Length Article

Surface and quantum chemical parameters of nickel oxide nanostructures suited for ultraviolet-assisted cationic dye degradation

G. Rathika [a], R. Jagadeeswari [b,*], T. Sathiyapriya [c], P. Selvakumar [d]

[a] Dept. of Chemistry, PSG College of Arts & Science, Coimbatore, 641014, Tamil Nadu, India
[b] Dept. of Chemistry, KPR Institute of Engineering and Technology, Coimbatore, 641407, Tamil Nadu, India
[c] Dept. of Chemistry, Coimbatore Marine College, Coimbatore, 641032, Tamil Nadu, India
[d] Dept. of Humanities and Sciences, Gokaraju Rangaraju Institute of Engineering and Technology, Hyderabad, 500090, Telangana, India

ARTICLE INFO

Keywords:
Nickel oxide nanoparticles (NiO NPs)
Photodegradation
Surface parameters
Optical band gap
Density functional theory (DFT)

ABSTRACT

Nickel oxide (NiO) nanostructures were synthesized through chemical precipitation and subsequently analyzed using a scanning electron microscopy (SEM) and X-ray diffraction (XRD). Rietveld refinement of XRD data revealed a cubic structure with lattice parameters of a = b = c = 4.173 Å. Fourier transform infrared spectroscopy and energy dispersive X-ray were employed to analyze the functional group and elemental composition of NiO NPs. The ultraviolet diffuse reflectance spectra indicated an optical band gap of 3.08 eV for synthesized NiO nanoparticles. Surface characteristics were evaluated using the Gwyddion open-source application, and parameters including Ra (mean roughness), Rq (mean square roughness), Rsk (surface skewness), and Rku (kurtosis coefficient) were calculated. The chemical properties of NiO were investigated through density functional theory calculations, and the results aligned well with experimental data. Furthermore, a comparative analysis of the photodegradation of methylene blue (MB) and rhodamine B (RhB) in the presence of UV light was examined, and it followed pseudo-first-order rate kinetics with degradation efficiencies of 82.62% (MB) and 71.31% (RhB), respectively. The electric energy per order for the photodegradation process was calculated to be 9.4×10^2 kWh/m^3/order (MB) and 11.7×10^2 kWh/m^3/order (RhB). Notably, the low electric energy consumption per order indicated a cost advantage for the reactor setup.

1. Introduction

Increasing environmental pollution is a direct result of industrialisation and population expansion. Pollutants present in the environment often act as carcinogens and mutagens, posing substantial challenges to their removal from the environment. In the context of polluted waterways, the primary pollutants can be categorised into azo and non-azo dyes based on the presence or absence of -N=N-(azo) groups in the dye structure (Kapoor et al., 2021). Cadmium sulphuric acid is used in 10%–15% of global dye manufacturing, and it is released into the environment by chemical and pharmaceutical industries (Yeamin et al., 2021). Various organic pollutants are present in the effluent of these factories, and these contaminants play a major role in degrading aquatic habitats. Decreases in photosynthetic responses result from the presence of dyes in wastewater. Some of these dyes are toxic and associated with the development of malignant neoplastic disorders, which pose a substantial threat to the health of both people and animals (Baines et al., 2021). The poisoning of industrial wastewater with methylene blue (MB) and rhodamine B (RhB) dyes, which exert negative effects on ecosystems, is a major cause of concern. In response to the increasingly stringent global environmental standards, new frameworks and techniques have been developed for the removal of organic contaminants and pigments from wastewater before its discharge. Various processes such as ion exchange, adsorption, membrane separation, and chemical precipitation/coagulation are often used to remove contaminants from wastewater discharge.

Photocatalysis involves the utilisation of ultraviolet (UV) or visible light to remove or break down organic pollutants, dyes, and microbes on surfaces (Ali et al., 2022). Photocatalysis, which occurs when light interacts with a semiconductor material, causes electrons to shift from the valence band (VB) to the conduction band (CB), creating superoxide anions that may efficiently engage in free radical reactions and hasten the degradation of dye molecules (Peng et al., 2019). Density functional theory (DFT), a computational tool rooted in quantum mechanics, is

* Corresponding author. Dept. of Chemistry, KPR Institute of Engineering and Technology, Coimbatore, 641407, Tamil Nadu, India.
E-mail addresses: r.jagadeeswari@kpriet.ac.in, jagadeeswarichem@gmail.com (R. Jagadeeswari).

https://doi.org/10.1016/j.kjs.2024.100200
Received 22 January 2023; Received in revised form 25 August 2023; Accepted 29 January 2024
Available online 19 February 2024

used to examine the electrical structure of molecules. Within this framework, electron density is used to determine the characteristics of a system with numerous electrons (Verma and Truhlar, 2020). Nickel oxide semiconductor (p type) materials have attracted the attention of researchers due to their unique features, excellent electron transport capacity, high chemical stability, electrocatalytic activity, and superconductive nature (Yi et al., 2020). Nickel oxide has diverse possible uses, including in water purification, gas detection, electrochemical performance improvement, and microbial infection prevention. Nickel oxide nanoparticles (NiO NPs) fabricated using different physical and chemical processes have been reported (Ariyanta et al., 2021). A chemical sensor containing active CuO NiO NPs can serve as a highly sensitive and effective sensor for the detection of harmful compounds. It employs a robust IV technique for use in broad-scale environmental safety and healthcare sectors (Zeid et al., 2020). Using a self-assembly technique and a calcination procedure, a study synthesized carbon anion-layered Ni/NiO nanoparticles (NPs) and used them as electrocatalysts in the alkaline hydrogen evolution reaction (Yan et al., 2022). In a hydrotropic aqueous solution, a sonochemical synthesis of 3,4-dihydropyridine-2(1H) ones was achieved by employing agar-supported NiO NPs (Attar et al., 2023). Unique flower-shaped NiO NPs were demonstrated to be stable in water and recyclable, making them an effective material for detoxifying water contaminated with L-CHT herbicide (Iqbal et al., 2021). Variations in temperature in the synthesized NiO nanoparticles were examined using the solid-state combustion method; MB photodegradation was reported (Sumantha et al., 2021). NiO-CNT nanocomposites were synthesized and assessed for their potential as adsorbents by evaluating their effectiveness in removing methyl orange (MO) in the absence of a reducing agent when exposed to visible light (Alkallas et al., 2022). Furthermore, a comparative analysis of the effects of the morphologies and structures of NiO NPs as photocatalysts in environmental applications was performed (Mou et al., 2022). However, discrepancies in the capacity to generate reactive oxygen species (ROS) and the specific types of ROS produced by metal oxide NPs may contribute to the observed heterogeneity in their photocatalytic reactions. In addition, the photocatalytic outcomes of metal oxide NPs are considerably affected by their structural and physical characteristics (size, phase, surface area, and shape) and the production method employed (Narasimharao and Ali, 2020). Given the scarcity of the literature for comparison, this study was conducted to address this gap and provide a comprehensive comparison.

In this study, we synthesized nanocrystalline NiO by using a simple and direct precipitation method and examined its structural and morphological characteristics. The electronic distribution and structure of a nanosized photocatalyst (NiO) were determined using DFT calculations. Furthermore, the surface characteristics of NiO NPs were investigated for their potential efficacy in the degradation of cationic dyes such as MB and RhB. In addition, we examined both the reaction kinetics and the electrical energy required.

2. Materials and methods

Analytical research grade nickel nitrate hexahydrate ($Ni(NO_3)_2$. $6H_2O$), sodium hydroxide (NaOH), rhodamine B, and MB were purchased from Merck, Mumbai, India and used directly without further purification. All experimental solutions were prepared using double distilled (DD) water.

2.1. Preparation of NiO catalyst through precipitation

$Ni(NO_3)_2$. $6H_2O$ (0.1 M) solution was prepared by dissolving it in deionised water. Drop by drop, an aqueous solution of NaOH solution (0.8 M) was added to the aqueous solution of nickel nitrate, and the mixture was stirred for 6 h at 80 °C. Slowly, a green-coloured precipitate was obtained and washed several times with DD water and ethanol. The obtained solid was dried initially at 120 °C. Then, NiO NPs were annealed for 5 h at 500 °C. Finally, the obtained black NiO NPs were collected and used for further research.

2.2. Catalyst characterisation and measurements

X-ray diffraction (XRD) experiments were performed using an X-ray diffractometer (Rigaku D max-C), and CuKα radiation (1.5406Å) was employed to determine the crystal structure of NiO NPs. The morphology and elemental content of NiO NPs were examined using a scanning electron microscope with energy dispersive X-ray (SEM with EDX, Sirion). In addition, the surface roughness was analyzed using the free programme Gwyddion. Using Gwyddion 2.58, the SEM images of NiO NPs were transformed into three-dimensional images. Subsequently, the following roughness characteristics were determined: mean roughness (Ra), mean square roughness (Rq), surface skewness (Rsk), and kurtosis coefficient (Rku) (Trovato et al., 2022). The ultraviolet diffuse reflectance (UV-DRS-JASCO V570) spectrophotometer was employed to record the absorption spectrum of NiO NPs.

2.3. Density functional theory (DFT) studies

The GAUSSIAN 09 programme was employed to perform the quantum chemical computations of NiO atoms (Hassan et al., 2021). In addition, Gauss view 6 was used for both building molecular structures and visualising them in three dimensions (Ahmed and Hashim, 2021). The ground-state molecular structure was built initially, with further geometry optimisation yielding the NiO molecule (linear) and a bond length of 1.60 Å (Fig. 1). In DFT, the B3LYP exchange functional (Becke's three-parameter hybrid) was used for fundamental computations and a 6-31 + G basis set (Zhurko et al., 2021). The same basis set was used for the highest occupied molecular orbital and lowest unoccupied molecular orbital (HOMO–LUMO) calculations, electrostatic potential (ESP), and global chemical reactivity descriptor (GCRD).

2.4. Photocatalytic studies

A specially designed photocatalytic reactor system made of wooden chambers was used in photodegradation experiments. Philips TUV-08 UV light (15W, $\lambda = 365$ nm) was placed inside the wooden enclosure. Then, the NiO catalyst (30 mg) was dissolved in 30 mL of 3×10^{-5} M aqueous dye solution (RhB and MB). After being stirred for 10 min, the solution was left undisturbed for an additional hour in the dark to reach

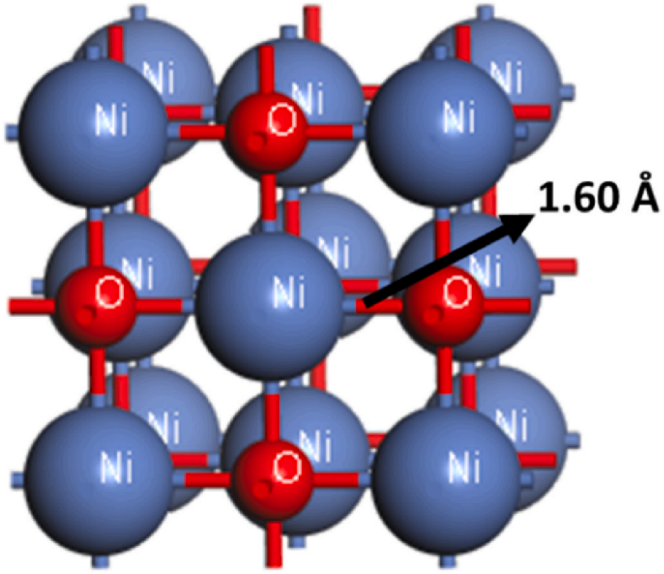

Fig. 1. Structure of nanocrystalline NiO.

the adsorption equilibrium. Once the sample solution was ready, for 90 min at room temperature, the NiO NPs dye solution was subjected to UV light. Using a UV-Vis spectrophotometer, the degradation of these dyes was examined by collecting 5 mL of the samples at regular intervals and filtering the catalyst through a polyvinyl difluoride syringe filter (0.45 μm).

By measuring the optical absorption of MB at 663 nm and 554 nm for RhB, a concentration standard curve was plotted to estimate the strength of dye in the solution. From 0 to 90 min of irradiation, a linear decrease in the rate of decolourisation was observed, which corresponded to the reduction of absorption peak intensity in the visible region. Utilising the formula below, the decolourisation efficiency was computed (equation (1)) (Nechita et al., 2021).

$$\%\ \text{Degradation}\ (\eta) = [1 - C_t / C_0]\ X\ 100 \tag{1}$$

where C_0 is the initial concentration of the dye and C_t is the concentration of dye solution at different time intervals.

3. Result and discussion

3.1. Fourier transform infrared (FTIR)

Calcined nanomaterials tend to physically absorb water, reducing and broadening the O-H stretching vibration band that generates a wide band of absorption centred at 3419 cm^{-1} (Boudiaf et al., 2021). At 500 °C, the calcination process removed CO_2 from the material, eliminating the peak at 2385 cm^{-1}. This finding aligns with that of a previous study (Abd-Elnaiem et al., 2022). Additionally, we observed a weak band with a wavelength of 1625 cm^{-1}, which corresponded to the H-O-H bending vibration (Sharma et al., 2021). The peak at 1382 cm^{-1} was attributed to the OH group's stretching vibration (Sharma et al., 2021). The intensity of NiO stretching vibrations was observed at 488 and 675 cm^{-1} (Abd-Elnaiem et al., 2022), and the wide absorption intensity indicated the nanocrystalline nature of NiO particles. Because the crystallite size of prepared nickel oxide NPs was smaller than that of the bulk form, the NiO stretching vibration shifted towards blue, as observed in the FTIR spectrum of NiO NPs (Fig. 2). Because of their spherical nanostructures and quantum size effect, NiO NPs absorb light at longer wavelengths in the FTIR spectrum than their bulk form.

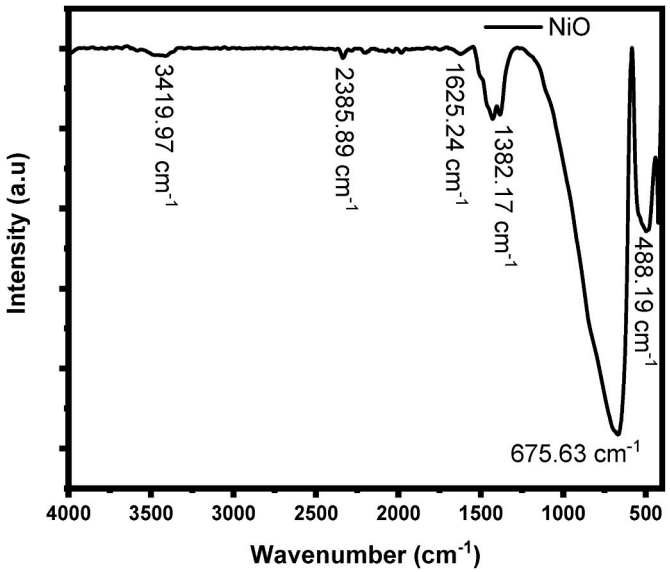

Fig. 2. Fourier transform infrared (FTIR) spectra precipitated NiO NPs.

3.2. Bandgap calculation

The UV-DRS of NiO NPs was measured in the wavelength range of 200–800 nm (Fig. 3a). A wide absorption peak was noted between 200 and 400 nm in DRS absorption spectra, and the optical band gap of produced NiO NPs was evaluated using Tauc's equation (Kaya et al., 2021).

$$[F(R)h\upsilon/t]^{1/n} = A\ (h\upsilon - E_g) \tag{2}$$

where F(R)-Kubelka–Munk function (Shkir et al., 2021) (F(R) = (1 R)^2/2R), 't' is the thickness of the material, R is the reflectance of the spectrum (n-band gap transition), A is the proportional constant, and $h\upsilon$ is photon energy. Fig. 3b depicts Tauc's plot showing the relationship between energy and [F(R) $h\upsilon$]^2. A tangent line was drawn to meet the X axis. As shown in Fig. 3b, the band gap energy (Eg) of NiO NPs was determined to be 3.08 eV.

The following equation may be used to compute the valence band (VB) edge potential of a semiconductor at zero charge.

$$E_{VB} = X - E^C + 0.5\ E_g \tag{3}$$

where E_{VB} is the VB edge potential, X is the semiconductor's electronegativity, E^c is the energy of free electrons on the hydrogen scale (approximately 4.5 eV), and E_g is the semiconductor's band gap energy. The conduction band (CB) edge potential (E_{CB}) can be calculated using the formula $E_{CB} = E_{VB} - E_g$. The 'X' value of NiO was approximately 6.585, and its E_{VB} and E_{CB} values were 3.625 eV and 0.545 eV, respectively. Changes in the band gap energy and blue shift in the UV-vis spectrum strongly indicated the reduction in the particle sizes of the catalyst.

3.3. Powder X-ray diffraction

Powder X-ray diffraction (PXRD) is a crucial method used to determining the structure, element phase, and element type present in NiO NPs. In addition, the crystallite size of NiO NPs may be determined using PXRD. Diffraction patterns of NiO NPs were observed, with 2 θ values ranging from 20° to 80° (Fig. 4). According to the PXRD pattern, peaks emerged at the angle 2 θ of (37.26°, 43.31°, 62.9°, 75.42°, and 79.38°), which corresponded to the planes (111), (200), (220), (311) and (222) and correlated well with JCPDS (Joint Committee Powder Diffraction Standards Data) card no.00-004-0835 (Abioye et al., 2019). This result indicated that the produced NPs contain an NiO phase and a face-centred cubic crystal structure. The peak's strength and sharpness demonstrated the crystalline nature of NiO NPs. In addition, no other peaks were found, indicating the purity of NiO NPs. Using the standard Scherrer formula (Abioye et al., 2017), we determined the average crystallite size of as-prepared NiO NPs to be 27.2 nm. The formula is presented below:

$$D = \frac{K\lambda}{\beta\ cos\ \theta} \tag{4}$$

where D is the average crystallite size, λ is the wavelength of the incoming radiation (in this case, CuKα with a wavelength of 1.540 Å), K is a constant (0.89), often known as the shape factor, β is the FWHM (full width half maximum), and θ is the diffraction angle. Using the formula provided below (equation (5)) (Sharma and Kalita, 2022),

$$\delta = \frac{1}{D^2} \tag{5}$$

the computed dislocation density (δ) was found to be 1.351 × 10^{15} and the occurrence of dislocation density substantially affected the characteristics of NiO NP crystals. The PXRD strain was evaluated using the Williamson–Hall formula ($\varepsilon = \beta\cos(\theta)/4$) (Raeisi-Kheirabadi et al., 2021). Stress was determined from strain according to Hooke's law (σ =

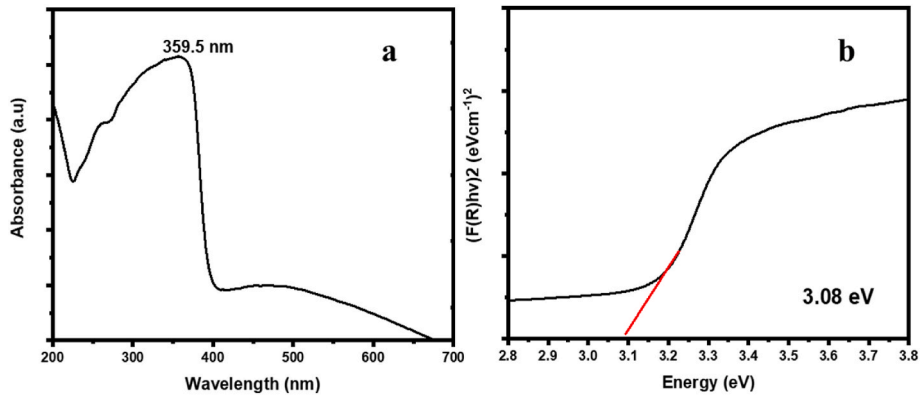

Fig. 3. a. Absorbance Spectra **b.** Tauc's Plot for precipitated NiO NPs.

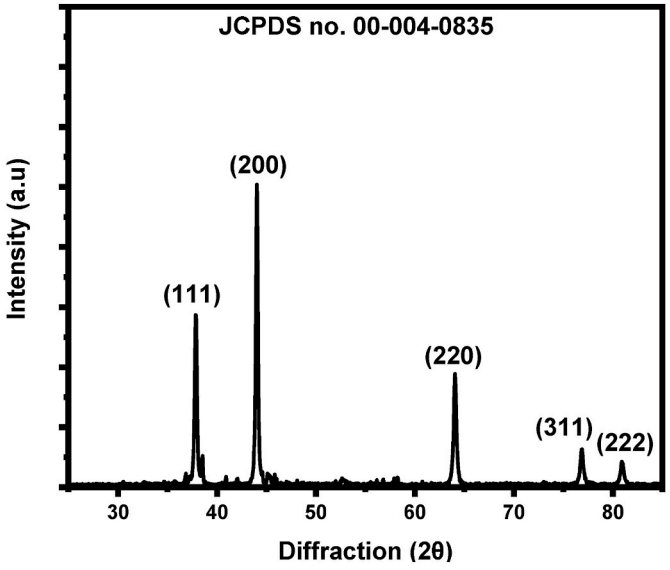

Fig. 4. X-ray diffraction (XRD) patterns of precipitated NiO NPs.

Cε), where 'C' is the bulk Young's modulus (1.46 ± 10^{10} N/m^2). The values of strain and stress were 0.0012 and 18.52 MPa for NiO NPs, respectively. Furthermore, the X-ray density was evaluated using equation (6) and found to be 6.85 g/cm^3

$$\rho = \frac{nA_w}{V_{cell}N_A} \tag{6}$$

where A_w is the atomic weight, n is the effective number of atoms per unit cell, V_{cell} is the volume of unit cell (for cubic a^3), and N_A is Avogadro's number.

The NiO active surface area (S) was determined using the Sauter formula (Abd-Elnaiem et al., 2022) (equation (7)):

$$S = 6000/D_\rho \tag{7}$$

where 'ρ' is the density of NiO NPs. The aforementioned equation is appropriate only for spherical particles. For NiO, the optimum calcination temperature and time result in a crystallite size of 27.2 nm.

The maximum equivalence surface area was 32.29 m^2/g. Agglomeration between surrounding NiO NPs increased the grain size, whereas the particle divider reduced the crystallite size. NiO NP size distribution broadened as a function of calcination temperature. NiO NPs were formed with a wider particle size dispersion due to calcination temperature (Abd-Elnaiem et al., 2022).

Various aspects of the XRD pattern, such as peak shift, peak broadening, and peak asymmetry, can be employed with the Rietveld refinement technique (Ahmed et al., 2021) to analyze the crystal structure of the investigated material. In this study, Rietveld refinement was performed on experimentally observed XRD data by using the GSAS-II program to investigate the effect of the synthesis process on structural parameters (Fig. 5). A pseudo-Voight function that uses integrated diffraction peaks as a function of structural characteristics was employed. The Marquardt least squares approach for data refining can be used to reduce differences between expected and observed patterns. Refinement provides exact fittings for peaks observed for the standard patterns of pure NiO (JCPDS card no.00-004-0835) with negligible refinement errors (Thrope et al., 2022). Fig. 5 illustrates the model crystal structure developed using Rietveld refinement settings. The improved parameters and estimated significant factors are listed in Table 1.

3.4. Scanning electron microscopy (SEM) and energy dispersive X-ray (EDX)

As observed in SEM images (Fig. 6a), NiO NPs tended to agglomerate, resulting in an irregular spherical form with particles of varied sizes (Fig. 6b). With a large surface area, these NPs perform efficiently in photocatalytic assays (Mashayekhi, 2022). The three-dimensional representation of the SEM image revealed nanoscale growth sites distributed across the surface (Fig. 6c). Furthermore, several crystallites with a pointed cone shape were identified. EDX analysis (Fig. 6d) confirmed that the synthesized NiO NPs comprise Ni and O atoms only. The elemental mapping of NiO NPs (Fig. 6e and f) confirmed the distribution of these elements. The absence of other contaminants in the spectrum of NiO NPs demonstrated the purity of NiO NPs (Ramu et al., 2021). The precise atomic proportions observed were Ni (55.2%) and O (44.8%).

3.5. Surface roughness of the catalyst

Gwyddion is an SEM analysis approach that is both user-friendly and compatible with several platforms. Gwyddion offers four parameters for assessing surface features: the mean roughness (Ra) of NiO NPs; the mean square roughness (Rq), which indicates modifications in the NiO NPs surface roughness; the surface skewness (Rsk), which demonstrates the surface height distribution symmetry of NiO NPs, and the kurtosis coefficient (Rku), which describes the 3D view of results depicting the surface structure on the plane (Fig. 6c) along with the loaded 2D photographs indicating surface heights (Fig. 6a). The Ra, Rq, Rsk, and Rku are only a few surface roughness metrics that can be obtained using the Gwyddion software (Table 2). The Ra value of NiO NPs was 49 nm, indicating that the produced particles had a rough surface due to the increased height caused by the calcination process (Bueno et al., 2022). The average Rq value of NiO NPs was 53.9 nm. A negative surface skewness (Rsk) value of −0.09 implied the presence a higher proportion

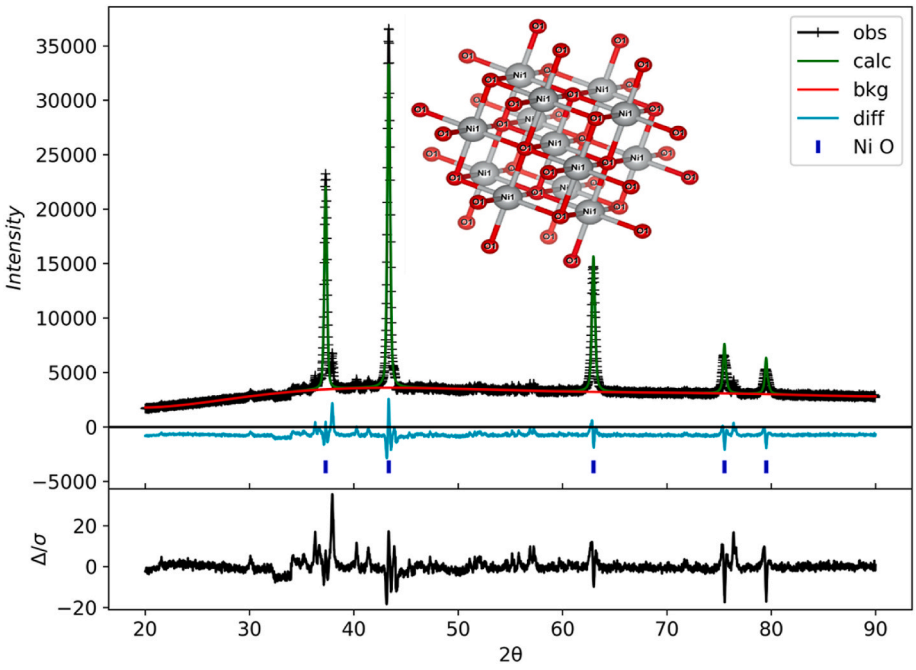

Fig. 5. Rietveld refinement of precipitated NiO NPs.

Table 1
Rietveld refinement parameters of NiO NPs.

Structural parameters	Rietveld refined		
Crystal Structure	Cubic		
Lattice constant (Å) a = b = c	4.173		
Unit-cell volume ($Å^3$)	72.69		
Space group	f m -3m		
Density (g/cm^3)	6.848		
χ^2	15.21		
Rwp (%)	5.078		
RF (%)	3.65		
Rp (%)	7.81		
Atomic Position	x	y	z
Ni1	0	0	0
O1	0.5	0.5	0.5

of troughs (low points) than peaks (high points; i.e. the NiO surface area was more). NiO NPs had a Rku value of 3.3, which was used to graphically represent the wavy characteristics of surface height distribution. Table 2 displays values obtained using the threshold surface mask and watershed to determine pore height. The pore size and grain size distribution were not uniform. Rough surfaces are often more effective in interacting with liquids and solids due to their larger contact area.

The activity of NiO NPs was proportional to their size and shape. According to UV-DRS measurements, the bandgap energy was 3.08 eV. The surface area was considerably affected by shape. In addition, the SEM findings of surface roughness supported the superior activity of NiO NPs. Because adsorption is the initial step of the photocatalytic process, the dye moiety readily adheres to the surface of the catalyst if the roughness is high due to poor crystallinity. The determined Ra and Rq of the prepared NPs were approximately 41.9 nm and 53.9 nm, respectively. The findings demonstrated that the photocatalytic activity and other catalytic-like activities depend on the particle size, surface area, and shape of NPs.

3.6. Quantum chemical studies

Because of electron donor–acceptor properties, the molecular orbitals (HOMO–LUMO) play a pivotal role in determining electronic transitions and structures. Fig. 7 presents the ground-state molecular geometries (optimised) together with the 3D plots of the LUMO, HOMO, $LUMO^{+1}$, and $HOMO^{-1}$ of the photocatalyst (NiO), representing band variances and atomic labels. Table 3 displays corresponding energy values. To examine the molecular orbitals of NiO atoms in three dimensions, we used the Gauss view programme in conjunction with a checkpoint file obtained from the DFT system. The green and red signals depict negative and positive actions, respectively. The oxygen molecule's highest molecular orbitals are located in the direction of the nickel atom. The HOMO–LUMO energy gap was 2.27 eV, whereas the energy gap between $LUMO^{+1}$ and $HOMO^{-1}$ was 3.33 eV. HOMO and LUMO orbital densities are shown in Fig. 7. The energy band gap of 3.08 eV, observed experimentally, was close to the calculated electronic excitation energy of 2.27 eV (Harun et al., 2020). The HOMO–LUMO calculations demonstrated that the produced NiO NPs are suitable for use as photocatalysts in waste degradation.

3.7. Electrostatic potential studies

Electrostatic potential (ESP) is linked to electronic density and predominantly utilised for identification purposes in biological experiments and those involving hydrogen bonding interactions to predict sites and their comparative reactivities towards electrophilic sites. The ESP at the mapped surface is represented graphically by the colour of the plot. In Fig. 8, the red colour represents electron-rich locations (e.g. oxygen) and indicates attraction, whereas the blue colour represents electron-deficient areas (e.g. nickel) and indicates repulsion (Cosentino et al., 2020). The findings of ESP provided insights into the structural characteristic bond present between nickel and oxygen atoms that forms the molecules of nickel oxide.

3.8. Global chemical reactivity descriptor parameters

To determine the chemical reactivity and stability of NiO NPs, the global chemical reactivity descriptor (GCRD) parameters of NiO NPs, such as chemical potential (μ), chemical hardness (η), electronegativity (χ), chemical softness (S), and electrophilicity index (ω), were computed from HOMO and LUMO energy values. Using equations (8)–(12), we determined all GCRD parameters (Sumantha et al., 2021).

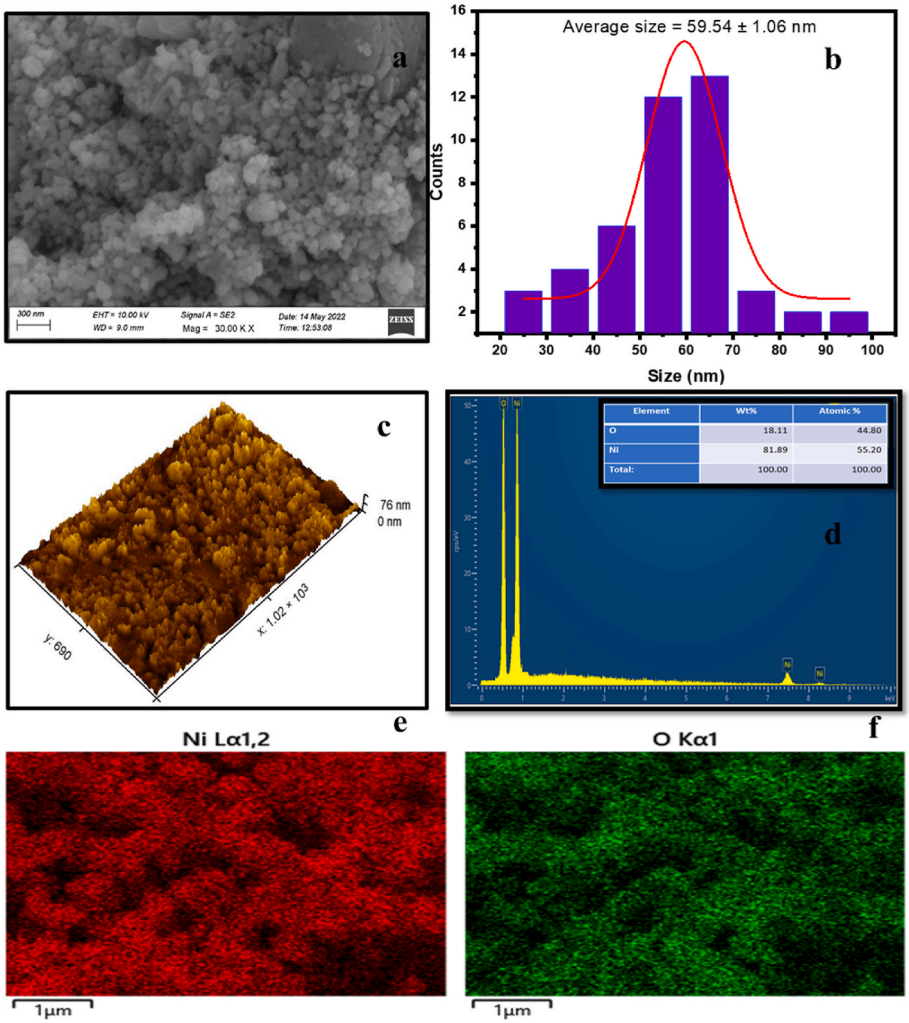

Fig. 6. a. SEM image; **b.** SEM-derived nanocrystal size; **c.** 3D SEM image; **d.** EDX spectra; **e, f.** Element mapping of NiO NPs.

Table 2
Grain structure and surface roughness parameters of NiO NPs.

Method	No. of. Grains	Plane grain %	Mean grain size (nm)	Mean grain area nm^2	Laplace grain volume μm^2	Roughness average (Ra) nm	Root mean square roughness (Rq) nm	Surface skewness (Rsk)	Kurtosis coefficient (Rku)
Threshold	3406	83.8	5.97	2680.9	424.4	41.9	53.9	−0.09	3.3
Watershed	33	0.370	18.19	1221.6	3.67				

$$\eta = (IP - EA)/2 \quad (8)$$

$$\chi = (IP + EA)/2 \quad (9)$$

$$\mu = -\chi \quad (10)$$

$$S = 1/2\eta \quad (11)$$

$$\omega = \mu^2/2\eta \quad (12)$$

where ionisation potential (IP) is $-E_{HOMO}$ and electron affinity (EA) is $-E_{LUMO}$. Table 4 presents the values of IP, hardness, electron affinity, chemical potential, electronegativity, electrophilicity index, and softness. The chemical reactivity changes were dependent on the molecular structure, as determined by several factors.

3.9. Photocatalytic activity

In the presence of UV light, the photocatalytic performance of NiO was investigated using RhB and MB dyes. Fig. 9 depicts the degradation of MB dye by NiO NPs at various time intervals. The prominent absorption peak of MB and RhB (663 and 554 nm, respectively) in absorption spectra declined gradually. In the presence of NiO NPs, more than 80% of MB dye was destroyed under UV light within 90 min. Fig. 9 also illustrates the effectiveness of NiO NPs in dye degradation. NiO NPs effectively degraded 82.62% of MB dye and 71.31% of RhB in 90 min (Fig. 10).

Fig. 11a presents the photodegradation of cationic dyes in the presence of NiO photocatalysts at pH levels ranging from 3 to 11. The cationic dyes and catalyst concentrations employed in this test are identical to those used in photodegradation studies. The highest efficiency was noted in a neutral medium (pH 7), whereas degradation rates were lower and visibility was higher in acidic and alkaline mediums (pH 3 and pH 11, respectively). Acidic environments (pH 3) inhibit

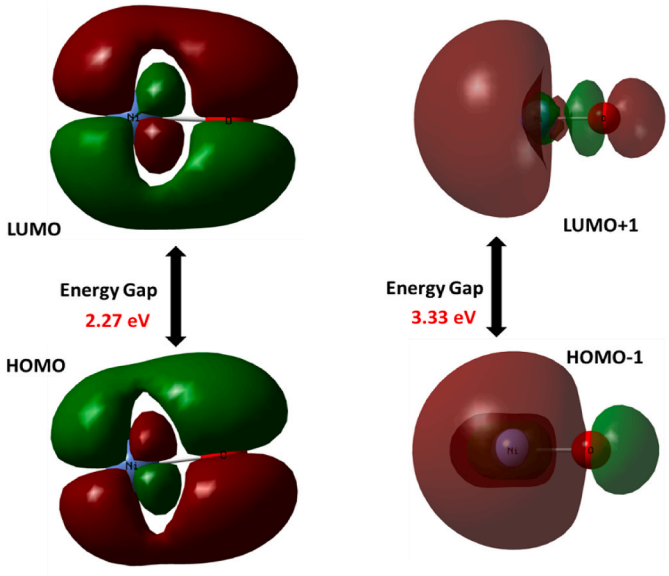

Fig. 7. Molecular orbitals and energy gaps (calculated) of linear NiO molecule.

Table 3
Energies of molecular orbital and energy gaps (calculated) of NiO NPs.

Energy orbitals	NiO NPs	
	In Hartress	In eV
HOMO	−0.2302	−6.265
LUMO	−0.1469	−3.997
Energy Gap	0.0833	2.27
$HOMO^{-1}$	−0.2269	−6.176
$LUMO^{+1}$	−0.1045	−2.844
Energy Gap	0.1224	3.33

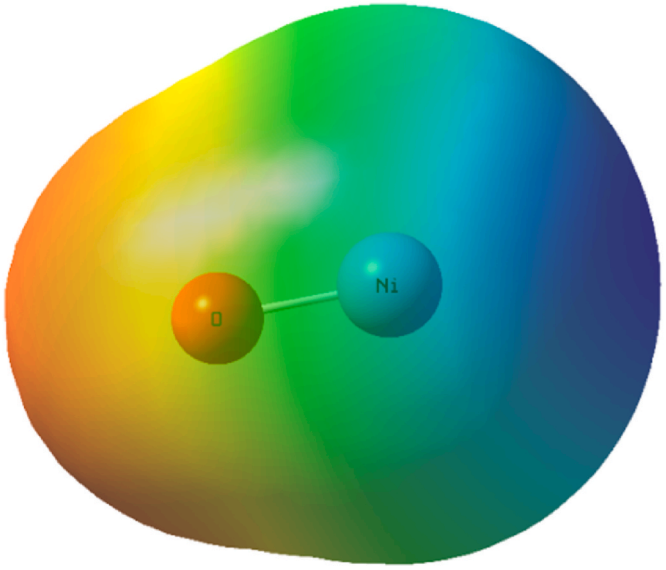

Fig. 8. Electrostatic potential (ESP) 3D plots of NiO NPs.

photodegradation because cationic organic dyes are repelled by the catalyst due to electrostatic repulsion. However, the decomposition process was inhibited at pH 11 (alkaline medium) because of substantial dye adsorption on the catalyst surface (Vidya and Balamurugan, 2019). Fig. 11b depicts the effects of catalyst quantity (10–40 mg) on cationic dye photodegradation (3×10^{-5} M). Because of an increase in the

Table 4
GCRD parameters of NiO NPs.

GCRD Parameters	NiO NPs	
	In Hartress	In eV
Chemical hardness (η)	0.0833	1.134
Chemical potential (μ)	−0.1885	−5.131
Chemical softness (S)	12.0	0.8818
Electronegativity (χ)	0.1885	5.131
Electrophilicity index (ω)	0.213	11.608

number of active surface sites for degradation processes, the percentages of MB and RhB degradation increased in proportion to catalytic quantity (Bhagwat et al., 2021). The initial dye concentrations varied from 2 to 5 $\times 10^{-5}$ M when the photocatalyst amount was maintained at 30 mg (Fig. 11b). Initially, the photodegradation increased and degradation efficiency decreased from 83% to 47% for MB and 70%–41% for RhB. Once the concentration of the dye was increased from 3×10^{-5} M to 5×10^{-5} M, UV light penetration on the NiO surface decreased, reducing the formation of active radicals (Bhagwat et al., 2021). The catalyst and dye concentrations were optimised as 30 mg and 3×10^{-5} M.

Initially, UV light was used to irradiate the surface of the NiO photocatalyst. Excited valence-band electrons migrate to the conduction band due to radiation. The generation of positive holes during electron transfer is proportional to the number of excited electrons, providing ideal conditions for the formation of pairs of holes (positive) and excited electrons (negative) (Abd-Elnaiem et al., 2022). The energy gap value substantially affects the photocatalyst's efficiency, as shown by the fact that the prepared NiO had the smallest energy gap value (3.08 eV), allowing more time for the reformation of resultant free radicals. Surface reactions continue as irradiation-generated conduction-band electrons and valence-band holes diffuse to the surface. Superoxide radical anions are produced when released electrons combine with oxygen. The isolated holes combine with water to produce OH radicals. Because their high reactivity, the produced radicals degrade the organic dye of preference. Furthermore, due to their capacity to convert the cationic dyes MB and RhB into environmentally friendly, harmless molecules, such as carbon dioxide and pollution-free water, the generated radicals serve as fundamental components in this photo-destruction process (Abd-Elnaiem et al., 2022).

3.10. Degradation mechanism and kinetic study

The greater photocatalytic activity of NiO NPs is attributable to the increase in the total surface area. This denotes the number of reactive sites (surface roughness) available on the NiO surface for the production of free radicals (Darbandi et al., 2021). The added cause for the increase in photocatalytic activity was the semiconductor's narrower band gap (3.08 eV), which enables it to produce further photons to stimulate electrons from the valence band to the conduction band (Sun et al., 2021). The arrangement of the electronic band structure of NiO NPs affects photocatalytic activity. To strengthen these findings, plausible degradation mechanisms and kinetic studies were conducted. The rough surface of NiO NPs contributes to dye photodegradation.

The comparative degradation efficiency of MB and RhB dyes is presented in Fig. 11. Fig. 12 depicts the relationship between concentration changes and reaction time. It also shows a schematic illustration of the photocatalytic generation of free radicals by NiO. The rate constant was determined using the following formula (equation (13)), and the degradation process follows the pseudo-first-order kinetics.

$$-ln\left[\frac{C}{C_0}\right] = kt \tag{13}$$

To determine the R^2 value and rate constant (k), a graph between ln (C/C_o) and response time was plotted. Furthermore, the R^2 value and rate constant (k) were 0.9445 and 0.0183 min^{-1} for MB, respectively,

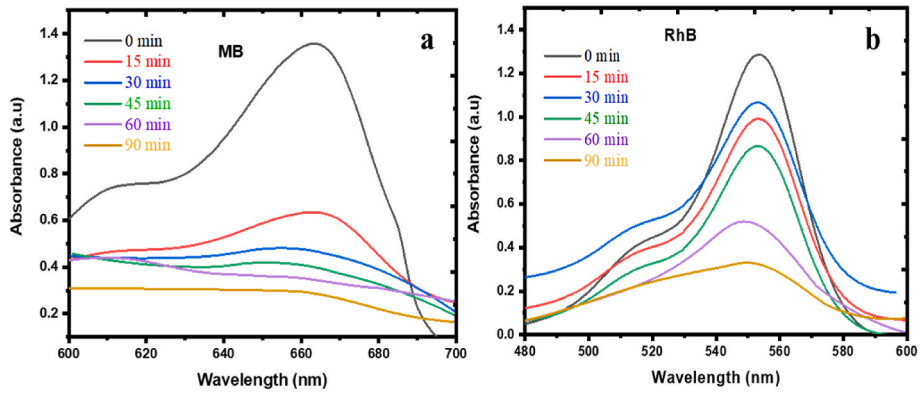

Fig. 9. a, b. Photocatalytic activity of precipitated NiO NPs against MB and RhB under UV light.

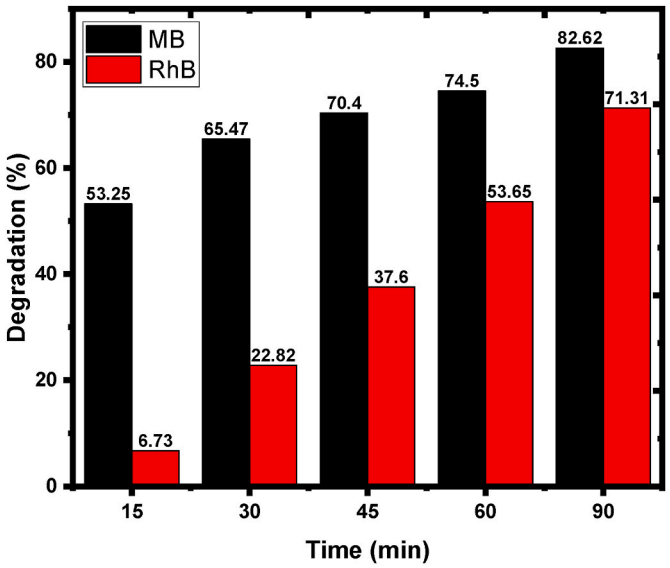

Fig. 10. Degradation efficiency of MB and RhB under UV light by NiO NPs.

and 0.9380 and 0.0147 min^{-1} for RhB, respectively.

3.11. *Electrical energy consumption and process efficiency*

Consumption of electricity is a significant factor in the overall cost of running a photocatalytic process. Electric energy per order (E_{EO}) may be introduced into a first-order kinetic photochemical process at low concentrations. This is the amount of electrical energy needed for the lamp, measured in kilowatt-hours (kWh), to treat a substrate by one order of magnitude in a unit volume (1 m^3) of polluted water or air by equation (14) (Kang et al., 2021):

$$E_{EO} = \frac{P_{el} t}{V \log\left[\frac{C}{C_0}\right]} \tag{14}$$

where P_{el} (kW) and V (m^3) represent the amount of electricity used and the amount of aqueous solution, respectively, and t(h) represents the time required to reach concentration C from concentration C_0. When equations (13) and (14) are combined, the equation for the E_{EO} is obtained as

$$E_{EO} = \frac{P_{el} 2.303}{Vk} \tag{15}$$

For the photodegradation of MB and RhB, the predicted electrical energy values were 9.4 × 10^2 kWh/m^3/order and 11.7 × 10^2 kWh/m^3/order, respectively. Less electricity was required for degrading MB than for degrading RhB. The process efficiency of photodegradation can be determined using equation (16) (Bhatti et al., 2019),

$$\varphi = \frac{C_0 - C}{t\, I\, S} \tag{16}$$

where 'I' is the light intensity, which is measured in watts (15 W), and S is the solution exposed plane surface area (101 cm^2) at time t. Co and C represent the beginning and final concentrations of dye, respectively, and ppm per Einstein is used to quantify the process. The efficiency of MB and RhB degradation by NiO NPs was estimated to be 0.842 × 10^{-5} ppm/E and 0.569 × 10^{-5} ppm/E. The finding suggest that MB degradation is more productive than RhB degradation. The NiO photocatalyst demonstrated higher photocatalytic activity for the breakdown of MB over RhB because of its smaller crystallite size, adequate bandgap, and surface characteristics.

4. Conclusion

NiO NPs were synthesized through chemical precipitation, and their structural morphology was analyzed using XRD, UV-DRS, SEM, and EDX. The average particle size of NiO NPs determined using PXRD was 27.2 nm, which aligns with SEM results. The ascertained cubic crystal structure with the point group fm-3m of NiO was confirmed by the Rietveld method of XRD refining. The optical band gap of the prepared NiO NPs calculated from UV-DRS was 3.08 eV. The as-prepared NiO NPs were free from impurities, suggesting the purity of the sample, as evident from EDX analysis. The small size of particles and the narrow band gap of prepared NiO NPs were responsible for the photocatalytic removal of cationic dyes from aqueous solutions. Image characterisation with Gwyddion was applied on the SEM images of NiO NPs to determine surface parameters. The Ra and Rq values were determined to be 41.9 nm and 53.9 nm, respectively. The photocatalyst degraded 82.62% of MB and 71.31% of RhB within 90 min, respectively. Compared with RhB, MB had a higher affinity for NiO NPs and showed better degradation. DFT investigations of GCRD and HOMO–LUMO energies calculated by employing TD-DFT aligned with experimental results. The rate of photodegradation was characterised by pseudo-first-order reaction kinetics, and the comparatively low electrical energy consumption, 9.4 × 10^2 kWh/m^3/order for MB and 11.7 × 10^2 kWh/m^3/order for RhB, suggests significant savings in the intended use of the photoreactor.

Data availability statement

The datasets generated during and/or analyzed during the current study are available from the corresponding author upon reasonable request.

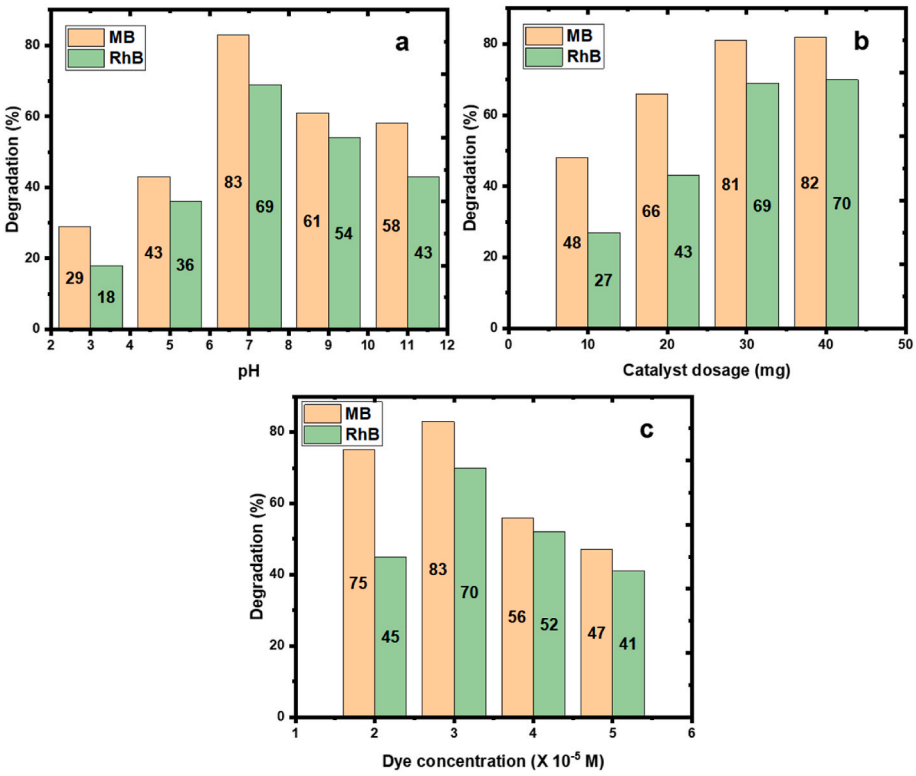

Fig. 11. Effect of **a.** pH, **b.** catalyst amount (mg), and **c.** initial dye concentration(M) for the degradation of MB and RhB by NiO.

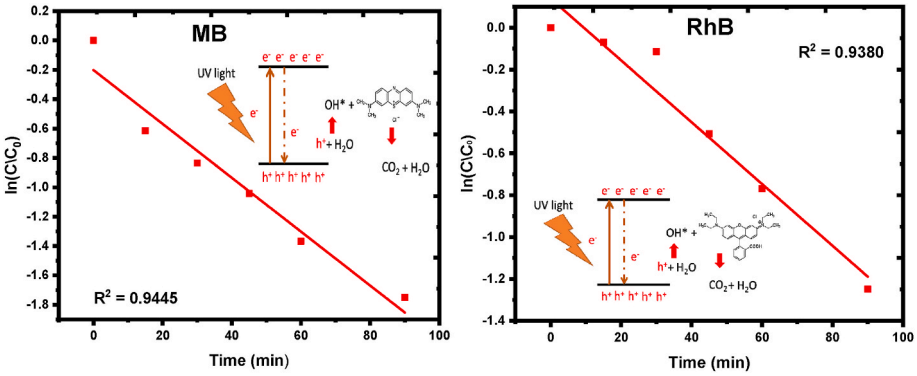

Fig. 12. a, b. Pseudo-first-order kinetics for the photocatalytic degradation of MB and RhB by precipitated NiO NPs.

Declaration of competing interest

The authors declare that they have no known competing financial interests or personal relationships that could have appeared to influence the work reported in this paper.

Acknowledgements

The authors are thankful to Dr. R. Saranya, Assistant Professor, Department of English, KPR Institute of Engineering and Technology, Coimbatore for her diligent proofreading of this research article.

References

Abd-Elnaiem, A.M., Hakamy, A., Ibrahem, I.A., Ali, A.M., Mohamed, W.A., Abo Zeid, E. F., 2022. Thermal-induced effects on the structural and photocatalytic properties of Nickel Oxide nanoparticles for Indigo Carmine dye removal. J. Inorg. Organomet. Polym. Mater. 32, 2209–2220.

Abioye, A.M., Noorden, Z.A., Ani, F.N., 2017. Synthesis and characterizations of electroless oil palm shell based-activated carbon/nickel oxide nanocomposite electrodes for supercapacitor applications. Electrochim. Acta 225, 493–502.

Abioye, A.M., Abdulkadir, L.N., Ani, F.N., 2019. Effect of calcination conditions on the supercapacitive performance of activated carbon/nickel oxide nanocomposite electrodes prepared by electroless nickel plating. J. Electron. Mater. 48, 3721–3735.

Ahmed, H., Hashim, A., 2021. Structural, optical and electronic properties of silicon carbide doped PVA/NiO for low cost electronics applications. Silicon 13, 1509–1518.

Ahmed, S.K., Mahmood, M.F., Arifuzzaman, M., Hossen, M.B., 2021. Enhancement of electrical and magnetic properties of Al3+ substituted CuZn nano ferrites with structural Rietveld refinement. Results Phys. 30, 104833.

Ali, H.M., Ibrahim, S.M., Zeid, E.F.A., Al-Hossainy, A.F., Abd El-Aal, M., 2022. A comparative study of Cu-anchored 0D and 1D ZnO nanostructures for the reduction of organic pollutants in water. RSC Adv. 12, 16496–16509.

Alkallas, F.H., Toghan, A., Ahmed, H.A., Alrefaee, S.H., Pashameah, R.A., Alrebdi, T.A., Mwafy, E.A., Mostafa, A.M., 2022. Catalytic performance of NiO nanoparticles decorated carbon nanotubes via one-pot laser ablation method against methyl orange dye. J. Mater. Res. Technol. 18, 3336–3346.

Ariyanta, H.A., Ivandini, T.A., Yulizar, Y., 2021. Novel NiO nanoparticles via phytosynthesis method: structural, morphological and optical properties. J. Mol. Struct. 1227, 129543.

Attar, S.R., Sapkal, A.C., Dhane, N.S., Kamble, S.B., 2023. Agar supported NiO NPs: a sustainable approach for synthesis of 3, 4-dihydropyrimidin-2 (1H)-Ones in aqueous hydrotropic media. Catal. Lett. 1–13.
Baines, C., Lerebours, A., Thomas, F., Fort, J., Kreitsberg, R., Gentes, S., Meitern, R., Saks, L., Ujvari, B., Giraudeau, M., 2021. Linking pollution and cancer in aquatic environments: a review. Environ. Int. 149, 106391.
Bhagwat, U.O., Kumar, K.R., Syed, A., Marraiki, N., Ponnusamy, V.K., Anandan, S., 2021. Facile hydrothermal synthesis of tungsten tri-oxide/titanium di-oxide nanohybrid structures as photocatalyst for wastewater treatment application. J. Cluster Sci. 1–10.
Bhatti, M.A., Shah, A.A., Almani, K.F., Tahira, A., Chalangar, S.E., dad Chandio, A., Nur, O., Willander, M., Ibupoto, Z.H., 2019. Efficient photo catalysts based on silver doped ZnO nanorods for the photo degradation of methyl orange. Ceram. Int. 45, 23289–23297.
Boudiaf, M., Messai, Y., Bentouhami, E., Schmutz, M., Blanck, C., Ruhlmann, L., Bezzi, H., Tairi, L., Mekki, D.E., 2021. Green synthesis of NiO nanoparticles using Nigella sativa extract and their enhanced electro-catalytic activity for the 4-nitro-phenol degradation. J. Phys. Chem. Solid. 153, 110020.
Bueno, V., Bosi, A., Tosco, T., Ghoshal, S., 2022. Mobility of solid and porous hollow SiO2 nanoparticles in saturated porous media: impacts of surface and particle structure. J. Colloid Interface Sci. 606, 480–490.
Cosentino, S., Urso, M., Torrisi, G., Battiato, S., Priolo, F., Terrasi, A., Mirabella, S., 2020. High intrinsic activity of the oxygen evolution reaction in low-cost NiO nanowall electrocatalysts. Mater. Adv. 1, 1971–1979.
Darbandi, M., Eynollahi, M., Badri, N., Mohajer, M.F., Li, Z.-A., 2021. NiO nanoparticles with superior sonophotocatalytic performance in organic pollutant degradation. J. Alloys Compd. 889, 161706.
Harun, K., Salleh, N.A., Deghfel, B., Yaakob, M.K., Mohamad, A.A., 2020. DFT+ U calculations for electronic, structural, and optical properties of ZnO wurtzite structure: a review. Results Phys. 16, 102829.
Hassan, H.B., Abduljalil, H.M., Hashim, A., 2021. Augmented the structure, electronic and optical characteristics of PEO doped NiO for electronics applications. Phys. Chem. Solid State. 22, 501–508.
Iqbal, A., ul Haq, A., Cerrón-Calle, G.A., Naqvi, S.A.R., Westerhoff, P., Garcia-Segura, S., 2021. Green synthesis of flower-shaped copper oxide and nickel oxide nanoparticles via capparis decidua leaf extract for synergic adsorption-photocatalytic degradation of pesticides. Catalysts 11, 806.
Kang, W., Chen, S., Yu, H., Xu, T., Wu, S., Wang, X., Lu, N., Quan, X., Liang, H., 2021. Photocatalytic ozonation of organic pollutants in wastewater using a flowing through reactor. J. Hazard Mater. 405, 124277.
Kapoor, R.T., Danish, M., Singh, R.S., Rafatullah, M., HPS, A.K., 2021. Exploiting microbial biomass in treating azo dyes contaminated wastewater: mechanism of degradation and factors affecting microbial efficiency. J. Water Process Eng. 43, 102255.
Kaya, D., Aydınoğlu, H.S., Tüzemen, E.Ş., Ekicibil, A., 2021. Investigation of optical, electronic, and magnetic properties of p-type NiO thin film on different substrates. Thin Solid Films 732, 138800.
Mashayekhi, F., 2022. The effects of molar ratio and calcination temperature on NiO nanoparticles' properties. Int. Nano Lett. 1–7.
Mou, J., Ren, Y., Wang, J., Wang, C., Zou, Y., Lou, K., Zheng, Z., Zhang, D., 2022. Nickel oxide nanoparticle synthesis and photocatalytic applications: evolution from conventional methods to novel microfluidic approaches. Microfluid. Nanofluidics 26, 1–20.
Narasimharao, K., Ali, T.T., 2020. Influence of synthesis conditions on physico-chemical and photocatalytic properties of rare earth (Ho, Nd and Sm) oxides. J. Mater. Res. Technol. 9, 1819–1830.
Nechita, M.T., Suditu, G.D., Puițel, A.C., Drăgoi, E.N., 2021. Differential evolution-based optimization of corn stalks black liquor decolorization using active carbon and TiO2/UV. Sci. Rep. 11, 1–12.
Peng, Q., Tang, X., Liu, K., Luo, X., He, D., Dai, Y., Huang, G., 2019. High-efficiency catalysis of peroxymonosulfate by MgO for the degradation of organic pollutants. Minerals 10, 2.
Raeisi-Kheirabadi, N., Nezamzadeh-Ejhieh, A., Aghaei, H., 2021. A brief study on the kinetic of the voltammetric behavior of the modified carbon paste electrode with NiO nanoparticles towards loratadine as a carboxylate-amidic drug compound. Microchem. J. 162, 105869.
Ramu, A.G., Kumari, M.A., Elshikh, M.S., Alkhamis, H.H., Alrefaei, A.F., Choi, D., 2021. A facile and green synthesis of CuO/NiO nanoparticles and their removal activity of toxic nitro compounds in aqueous medium. Chemosphere 271, 129475.
Sharma, S.K., Kalita, M.P., 2022. Microstructure analysis of NiO nanocrystals and enhanced photocatalytic activities of NiO-CdS nanocomposites. J. Mater. Sci. Mater. Electron. 33, 7824–7837.
Sharma, P.K., Singh, M.K., Sharma, G.D., Agrawal, A., 2021. NiO nanoparticles: facile route synthesis, characterization and potential towards third generation solar cell. Mater. Today Proc. 43, 3061–3065.
Shkir, M., Chandekar, K.V., Khan, A., Alshahrani, T., El-Toni, A.M., Sayed, M.A., Singh, A.K., Ansari, A.A., Muthumareeswaran, M.R., Aldalbahi, A., 2021. Tailoring the structure-morphology-vibrational-optical-dielectric and electrical characteristics of Ce@ NiO NPs produced by facile combustion route for optoelectronics. Mater. Sci. Semicond. Process. 126, 105647.
Sumantha, H.S., Rajagopal, S., Nagaraju, G., Shashank, M., Suresha, B.L., 2021. Facile and eco-friendly combustion synthesis of NiO particles for photodegradation studies. Chem. Phys. Lett. 779, 138837.
Sun, S., Shen, G., Chen, Z., Pan, L., Zhang, X., Zou, J.-J., 2021. Harvesting urbach tail energy of ultrathin amorphous nickel oxide for solar-driven overall water splitting up to 680 nm. Appl. Catal. B Environ. 285, 119798.
Thrope, B., Ferreira Lima, A.R., Pinto, A.H., 2022. From the periodic properties of metals to the Rietveld refinement of the pharmaceutical molecule naproxen: three remote experiments about X-ray diffraction. J. Chem. Educ. 99, 2055–2066.
Trovato, V., Mezzi, A., Brucale, M., Abdeh, H., Drommi, D., Rosace, G., Plutino, M.R., 2022. Sol-gel assisted immobilization of alizarin red S on polyester fabrics for developing stimuli-responsive wearable sensors. Polymers 14, 2788.
Verma, P., Truhlar, D.G., 2020. Status and challenges of density functional theory. Trends Chem 2, 302–318.
Vidya, J., Balamurugan, P., 2019. Photocatalytic degradation of methylene blue using PANi-NiO nanocomposite under visible light irradiation. Mater. Res. Express 6, 0950c8.
Yan, Y., Ma, Q., Cui, F., Zhang, J., Cui, T., 2022. Carbon onions coated Ni/NiO nanoparticles as catalysts for alkaline hydrogen evolution reaction. Electrochim. Acta 430, 141090.
Yeamin, M.B., Islam, M.M., Chowdhury, A.-N., Awual, M.R., 2021. Efficient encapsulation of toxic dyes from wastewater using several biodegradable natural polymers and their composites. J. Clean. Prod. 291, 125920.
Yi, T.F., Wei, T.T., Mei, J., Zhang, W., Zhu, Y., Liu, Y.G., Luo, S., Liu, H., Lu, Y., Guo, Z., 2020. Approaching high-performance supercapacitors via enhancing pseudocapacitive nickel oxide-based materials. Adv. Sustain. Syst. 4, 1900137.
Zeid, E.A., Nassar, A.M., Hussein, M.A., Alam, M.M., Asiri, A.M., Hegazy, H.H., Rahman, M.M., 2020. Mixed oxides CuO-NiO fabricated for selective detection of 2-Aminophenol by electrochemical approach. J. Mater. Res. Technol. 9, 1457–1467.
Zhurko, G.A., Fedorova, A.A., Belyakov, A.V., 2021. Computations of IR spectra of some transition metal carbonyls and model clusters of nickel oxide with carbon monoxide. J. Mol. Struct. 1241, 130439.